NJC

ROYAL SOCIETY OF CHEMISTRY

PAPER

View Article Online
View Journal | View Issue

Cite this: *New J. Chem.*, 2020, 44, 1054

Mechanochemical synthesis, luminescent and magnetic properties of lanthanide benzene-1,4-dicarboxylate coordination polymers $(Ln_{0.5}Gd_{0.5})_2(1,4\text{-}BDC)_3(H_2O)_4$; Ln = Sm, Eu, Tb†

Tarek Alammar, *[a] Ihor Z. Hlova,[b] Shalabh Gupta, *[b] Anis Biswas,[b] Tao Ma,[b] Lin Zhou,[b] Viktor Balema,[b] Vitalij K. Pecharsky[ab] and Anja-Verena Mudring *[abc]

Received 19th May 2019,
Accepted 8th November 2019

DOI: 10.1039/c9nj02583a

rsc.li/njc

Mechanochemical reactions of benzene-1,4-dicarboxylate (BDC^{2-}) and lanthanide carbonates, $Ln_2(CO_3)_3{\cdot}xH_2O$ (Ln = Sm, Eu, Gd, Tb) yield phase pure lanthanide coordination polymers, $(Ln_{0.5}Gd_{0.5})_2(1,4\text{-}BDC)_3(H_2O)_4$ with Ln = Sm, Eu, Tb, which are isostructural with $Tb_2(1,4\text{-}BDC)_3(H_2O)_4$ as confirmed by powder X-ray diffraction and vibrational spectroscopy. Upon excitation with UV light all three compounds display strong emissions, characteristic for the respective optically active lanthanide ion, namely, red for Eu^{3+}, green for Tb^{3+} and orange-red for Sm^{3+}. In case of the Tb^{3+}-containing compound, the energy difference between the triplet energy level of benzene-1,4-dicarboxylate ligand (BDC^{2-}) allows for the most efficient BDC^{2-}–Tb^{3+} energy transfer. As a consequence, an intense green luminescence with rather long lifetime (0.81 ms) and high quantum yield (22%) is observed after allowed excitation of the BDC^{2-} ligand. The compounds are paramagnetic with no onset of long range magnetic ordering down to liquid He temperatures.

Introduction

The synthesis of luminescent metal–organic frameworks (MOFs) with high fluorescence intensities, lifetimes and quantum efficiencies continues to be a challenging task.[1] However, such materials are of interest for a number of applications such as organic light emitting diodes,[2] fluorescent lighting,[3,4] luminescent probes for medical imaging,[5] luminescence thermometry,[6] chemical sensors,[7] and molecular magnetorefrigeration[8] to name a few. The best performing luminescent MOF materials rely on the emission of trivalent lanthanide ions, Ln^{3+}, which arise from intraconfigurational 4f–4f-transitions. This is advantageous as it leads to high color purity. At the same time, the transitions are forbidden, leading to low absorption coefficients and, thus, direct excitation of the Ln^{3+} ions is very inefficient.[9] However, employing a suitable linker system that can participate in luminescence sensitization can improve the materials through efficient light absorption by the linker and subsequent electronic energy transfer to the emissive Ln^{3+} ion. Often this sensitization process is referred to as the "antenna effect".[10]

A number of factors influence the efficiency of ligand-to-metal energy transfer such as the intersystem crossing efficiency of the sensitizer, the location of the ligand triplet state through which sensitization occurs with respect to the emitting state of the lanthanide ion, the spectral overlap, potential charge transfer states and the donor–acceptor distance.[11] Achieving high efficiency of ligand-to-metal energy transfer, hence, requires careful selection or design of suitable organic linkers including appropriate configuration and energy levels and coordination modes for the respective Ln^{3+} ion to support an efficient luminescence sensitization. A variety of luminescent MOFs have been prepared using these guidelines.[9] During these studies it has been realized that the luminescent properties such as the lifetime and quantum yield are influenced by the employed synthetic protocols, especially when non-conventional approaches like mechanochemical reactions are used.[12–14] Experience tells that mechanochemical synthesis leads to materials with unusual morphologies, small particle sizes and low crystallinity, and hence affects the emission and quantum yields which are sensitive to structural defects and impurity doping.[15] Recently, MIL-78 type frameworks were synthesized by our group by using a simple, solvent-free mechanochemical approach.[16,17] Advantages of this method include, but are not limited to the high conversion rates, simplicity of the experimental set up, exclusion of solvents and reasonably good scalability.[18–20] Therefore, here we

[a] *Department of Materials Science and Engineering, Iowa State University, Ames, IA 50011-2300, USA. E-mail: tarek.alammar@rub.de*
[b] *Ames Laboratory, Iowa State University, Ames, IA 500011-3020, USA. E-mail: shalabhg@ameslab.gov*
[c] *Department of Materials and Environmental Chemistry, Stockholm University, Svante Arrhenius väg 16 C, 106 91 Stockholm, Sweden. E-mail: anja-verena.mudring@mmk.su.se*

† Electronic supplementary information (ESI) available. See DOI: 10.1039/c9nj02583a

have adopted the mechanochemical approach for the preparation of metal–organic polymer structures, $(Ln_{0.5}Gd_{0.5})_2(BDC)_3(H_2O)_4$ with Ln = Sm, Eu and Tb, containing benzene-1,4-dicarboxylate (1,4-BDC) as a linker, and investigate the optical and magnetic properties of the as-synthesized compounds.

Results and discussion

The solid-state mechanochemical reactions between $Ln_2(CO_3)_3{\cdot}xH_2O$ and BDC (benzene-1,4-dicarboxylate) are typically complete after 2 h of milling with a 100% yield. The completion of reactions is judged by the absence of characteristic Bragg peaks from either of the precursors or any other crystalline intermediates (Fig. 1). This is a clear advantage over the classical hydrothermal synthesis where lower yield, such as 67% for the Tb compound have been reported.[21]

Rietveld refinement using the FULLPROF program of the XRD patterns confirm that, the as-synthesized MOFs are isostructural with $Tb_2(1,4\text{-BDC})_3(H_2O)_4$ (S1 in ESI†).[21] In all cases, satisfactory structural refinement was obtained based on the reported crystal structure for the $Tb_2(1,4\text{-BDC})_3(H_2O)_4$ yielding an overall refined composition of $(Ln_{0.5}Gd_{0.5})_2(BDC)_3(H_2O)_4$. The number of water molecules in the lattice was independently confirmed by TGA as described below.

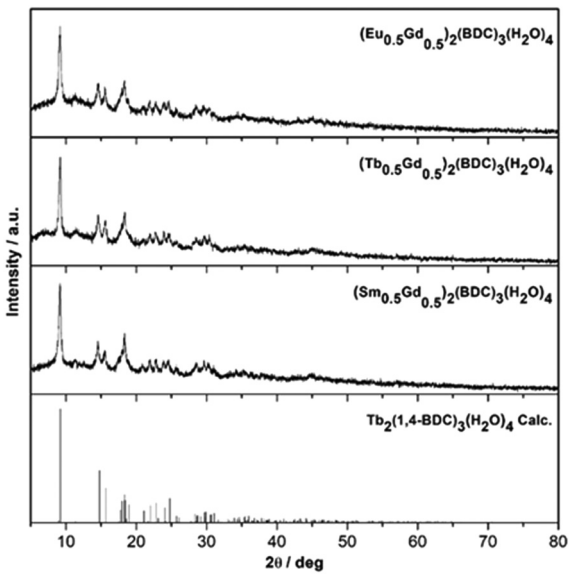

Fig. 1 Powder XRD patterns of mechanochemically prepared $(Ln_{0.5}Gd_{0.5})_2(1,4\text{-BDC})_3(H_2O)_4$, Ln = Eu, Tb, Sm and the calculated pattern of $Tb_2(1,4\text{-BDC})_3(H_2O)_4$ [ref. 21] (top to bottom).

The refined cell volumes range from 603.31(9) Å^3 for $(Tb_{0.5}Gd_{0.5})_2(BDC)_3(H_2O)_4$ to 607.0(1) Å^3 for $(Sm_{0.5}Gd_{0.5})_2(BDC)_3(H_2O)_4$ and the refined lattice constants are in excellent agreement with the changing ionic radius of the incorporated Ln^{3+} ions (ionic radii: Tb^{3+} = 92.3 pm, Eu^{3+} = 94.7 pm, Sm^{3+} = 95.8 pm) (Table 1).[22]

TG-DSC analyses of the as-prepared $(Ln_{0.5}Gd_{0.5})_2(BDC)_3(H_2O)_4$ MOFs display a two-step weight loss between room temperature and 1000 °C (Fig. 2). The first loss occurs at 100–215 °C. The weight losses are 8.4% (~4.1 eq. H_2O per f.u.) for Eu-, 8.7% (~4.2 eq. H_2O per f.u.) for Tb-, and 8% (~3.9 eq. H_2O per f.u.) for the Sm-containing MOF, which can be assigned to the dehydration of the as-synthesized samples. For all three samples, the second weight loss is observed at ~500 °C, which is caused by the thermal decomposition of $(Ln_{0.5}Gd_{0.5})_2(BDC)_3$, resulting in the formation of the respective lanthanide oxides.[23] This is in line with the results of previously reported thermal analysis of $Tb_2(BDC)_3(H_2O)_4$ and $Er_2(BDC)_3(H_2O)_4$.[21,24] No signals corresponding to the thermal events for benzene-1,4-dicarboxylic acid and/or carbonates can be seen, indicating complete consumption of the starting materials during the mechanochemical syntheses.

X-ray photoelectron spectroscopy (XPS) analyses were performed to examine the surface elemental composition and the oxidation state of each element in the mechanochemically synthesized $(Ln_{0.5}Gd_{0.5})_2(BDC)_3(H_2O)_4$. The XPS survey spectra for the different $(Ln_{0.5}Gd_{0.5})_2(BDC)_3(H_2O)_4$ materials are shown in Fig. 3, where all peaks corresponding to the characteristic electronic transitions of Sm, Eu, Gd, Tb, O and C are visible. Furthermore, XPS core level spectra of Eu-3d, Tb-3d, and Sm-3d regions are illustrated in Fig. 3. The XPS spectrum of $(Eu_{0.5}Gd_{0.5})_2(BDC)_3(H_2O)_4$ features two prominent peaks with binding energies of 1164.9 eV (Eu^{3+} $3d_{3/2}$) and 1135.1 eV (Eu^{3+} $3d_{5/2}$) together with three small satellites that occur at 1155.7 eV (Eu^{2+} $3d_{3/2}$), 1143.8 eV (mult), and 1125 eV (Eu^{2+} $3d_{5/2}$). The appearance of Eu^{2+} is related to the reduction of Eu^{3+} to Eu^{2+} as a result of the charge compensation procedure during profiling under the experimental

Table 1 Unit cell parameters and cell volumes for $(Ln_{0.5}Gd_{0.5})_2(1,4\text{-BDC})_3(H_2O)_4$ Ln = Sm, Eu, Tb

	a, *b*, *c*/Å	*α*, *β*, *γ*/°	*V*/Å^3
$(Sm_{0.5}Gd_{0.5})_2(BDC)_3(H_2O)_4$	6.2145(9) 10.098(2) 10.112(1)	101.93(1) 91.15(1) 101.57(1)	607.0(1)
$(Eu_{0.5}Gd_{0.5})_2(BDC)_3(H_2O)_4$	6.195(1) 10.090(2) 10.131(1)	102.05(1) 91.35(1) 101.34(1)	605.8(2)
$(Tb_{0.5}Gd_{0.5})_2(BDC)_3(H_2O)_4$	6.1936(4) 10.078(1) 10.1076(8)	102.114(7) 91.180(8) 101.460(7)	603.31(9)
$(Tb)_2(BDC)_3(H_2O)_4$ (See, ref. 21. Data from single crystal XRD)	6.2142(2) 10.0694(1) 10.0956(3)	102.247(2) 91.118(1) 101.518(2)	596.63(3)

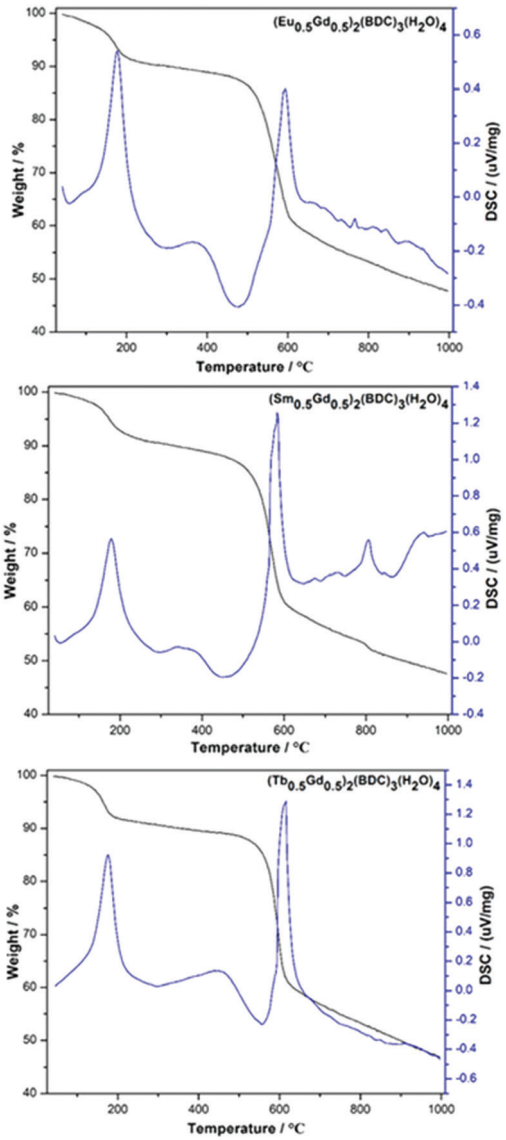

Fig. 2 TG-DSC curves of mechanochemically synthesized $(Ln_{0.5}Gd_{0.5})_2(BDC)_3(H_2O)_4$, Ln = Eu, Sm, Tb (top to bottom).

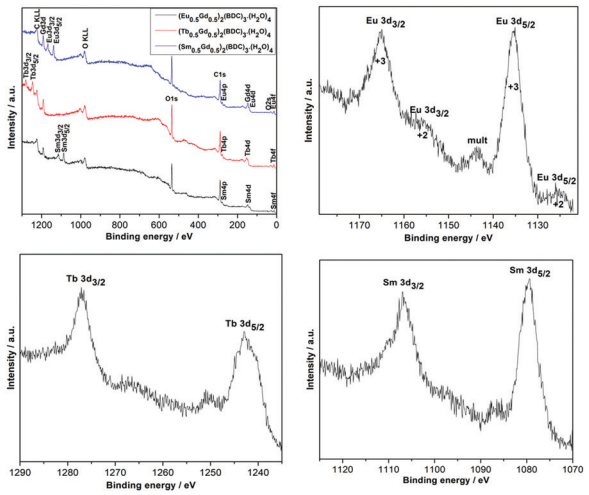

Fig. 3 X-ray photoelectron spectrum survey and narrow scans of Sm-3d, Eu-3d and Tb-3d regions for the $(Ln_{0.5}Gd_{0.5})_2(BDC)_3(H_2O)_4$ Ln = Sm, Eu and Tb.

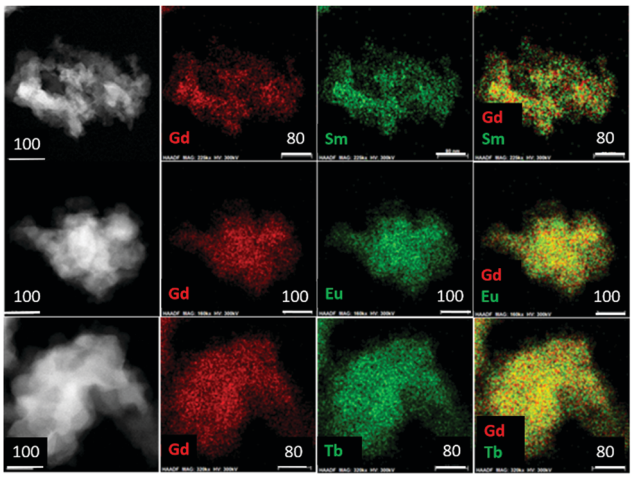

Fig. 4 High-angle-annular-dark-field scanning transmission electron microscopy images (extreme left) and corresponding EDS elemental mapping of the $(Ln_{0.5}Gd_{0.5})_2(BDC)_3(H_2O)_4$ Ln = Sm, Eu and Tb (top to bottom). White bars indicate dimensions in μm.

XPS conditions which is not unusual to notice for Eu(III) compounds.[25,26] The XPS spectrum of the core levels in the Tb-3d region of $(Tb_{0.5}Gd_{0.5})_2(BDC)_3(H_2O)_4$ displays two peaks at 1242.8 eV (Tb^{3+} $3d_{5/2}$) and 1277 eV (Tb^{3+} $3d_{3/2}$). Moreover, a satellite peak at 1250.8 eV was detected, which is ascribed to the existence of Tb^{4+} traces owing to oxidation of Tb^{3+} to Tb^{4+} during the measurement, which has been observed for other Tb^{3+} compounds under similar measurement conditions before.[27] The XPS spectrum of $(Sm_{0.5}Gd_{0.5})_2(BDC)_3(H_2O)_4$ shows two peaks centered at 1083.5 eV and 1111 eV. These peaks originate from Sm^{3+} $3d_{5/2}$ and Sm^{3+} $3d_{3/2}$ levels.

Electron microscopy reveals that the as-synthesized samples are composed of irregularly shaped and mostly aggregated particles (Fig. 4). A few particles ranging between 50–100 nm were selected for elemental mapping using energy dispersive spectroscopy (EDS) in order to ascertain the homogeneity of metal atoms in the heteronuclear complex compounds. Results are shown in Fig. 4 and Table 2. Element specific (Ln and Gd) images obtained from the same area are shown in two central columns and their combined color-composites are on the extreme right. The images clearly show a homogeneous distribution of metal atoms down to a few nanometers length scale, and shows no sign of

Table 2 Atomic and weight ratios of respective lanthanide ions with respect to gadolinium ions as determined by EDS in as-synthesized $(Ln_{0.5}Gd_{0.5})_2$(1,4-BDC)$_3(H_2O)_4$ MOFs Ln = Sm, Eu, Tb

Element	Wt%	At%	Error%
Gd/Sm	55.18/44.82	54.07/45.93	5.58/4.54
Gd/Eu	52.79/47.21	51.93/48.07	5.33/4.77
Gd/Tb	51.19/48.81	50.92/49.08	5.15/4.91

clustering or agglomeration of metal centres. These results demonstrate that mechanochemical methods can be effectively utilized to synthesize high quality luminescent MOFs where atomic level control, both chemistry and concentration, of emission centres are necessary to tailor and optimize quantum yields. As expected, the atomic ratios of Gd and respective lanthanide ions are close to 1 : 1.

Fig. 5 shows infrared (IR) spectra of $(Ln_{0.5}Gd_{0.5})_2(BDC)_3(H_2O)_4$ along with that of benzene-1,4-dicarboxylic acid for reference. Notably, the IR spectra of the three $(Ln_{0.5}Gd_{0.5})_2(BDC)_3(H_2O)_4$ samples are practically indistinguishable and confirm the formation of isostructural compounds. The absence of bands characteristic of the free acid *i.e.* the band at 1672 cm^{-1} which originates from the $\nu_{C=O}$ stretching band of COOH groups, the very broad O–H stretching band in the region between 2200 and 3200 cm^{-1}, and a band at around 1282 cm^{-1} which belongs to the bending vibration of carboxylic acid (δ_{O-H}), as well as the band at about 920 cm^{-1} attributable to OH out of plane bending in the IR spectra of $(Ln_{0.5}Gd_{0.5})_2(BDC)_3(H_2O)_4$ prove the complete deprotonation of COOH groups and the coordination of COO^- to Ln^{3+}. Also, the signals corresponding to the starting metal carbonates ($\nu_{C=O}$ between 1500 and 300 cm^{-1})[28–30] cannot be observed in the spectra of the final products. The bands in the range between 1501 and 1588 cm^{-1} and at 1386 cm^{-1} can be ascribed to asymmetric (ν_{as}) and symmetric (ν_s) stretching vibrations of $-COO^-$, respectively. The broad band centered at 3450 cm^{-1} corresponds to OH stretch of structural water molecule.[31]

The UV-Vis absorption spectra of benzene-1,4-dicarboxylic acid and as-synthesized $(Ln_{0.5}Gd_{0.5})_2(BDC)_3(H_2O)_4$ complexes (see ESI,† Fig. S2) were measured in the solid-state at room temperature. The absorption spectra of $(Ln_{0.5}Gd_{0.5})_2(BDC)_3(H_2O)_4$ and $Ln_2(BDC)_3(H_2O)_4$ are clearly dominated by features similar to those of benzene-1,4-dicarboxylic acid with bands occurring at 250 and 315 nm attributable to ligand centered and π–π* and n–π* transitions, respectively.[32] However, a bathochromic (red-) shift can be noticed between the transitions of the free acid and the coordination polymer, especially for the n–π* transitions, which underpins that BDC^{2-} is coordinating to the Ln^{3+} ions in the corresponding complexes.

The luminescent properties of the compounds were investigated at room temperature. Excitation spectra of $(Ln_{0.5}Gd_{0.5})_2(BDC)_3(H_2O)_4$ monitored at 616, 545, and 645 nm corresponding to the characteristically intense $^4G_{5/2}$–$^6H_{9/2}$, $^5D_0$–$^7F_2$ and $^5D_4$–$^7F_5$, transitions for Sm^{3+}, Eu^{3+} and Tb^{3+} are shown in Fig. 6. All recorded excitation spectra are dominated by a high intensity broad band between 240 nm to 323 nm corresponding to the π–π* and n–π* transitions of the ligand similar to the characteristic absorption spectra of the corresponding samples (ESI,† Fig. S2). In the excitation spectrum of $(Sm_{0.5}Gd_{0.5})_2(BDC)_3(H_2O)_4$ bands, which belong to the intraconfigurational 4f–4f transitions of Sm^{3+} can be detected, albeit with much weaker relative intensity. The most intense band centered at 405 nm originates from the $^6H_{5/2}$–$^4K_{11/2}$ transition of the Sm^{3+} ion. For $(Eu_{0.5}Gd_{0.5})_2(BDC)_3(H_2O)_4$, in addition to the broad absorption band, several low intensity narrow bands between 350 nm and 475 nm can be observed which can be assigned to the characteristic intraconfigurational 4f–4f transitions of Eu^{3+}.[33] The most intense bands are observed for the $^7F_0$–$^5L_6$ (394 nm) and $^7F_0$–$^5D_2$ transitions (465 nm). The excitation spectrum of $(Tb_{0.5}Gd_{0.5})_2(BDC)_3(H_2O)_4$ is clearly dominated by ligand-centered transitions and the characteristic transition for Tb^{3+} are barely visible. At 487 nm the $^7F_6$–$^5D_5$ transition can be weakly seen. Below 380 nm the transitions from $^7F_6$ to the ^5L and ^5G manifolds are barely visible. The comparatively weak intensities of the intraconfigurational f–f transitions of the Ln^{3+} ions compared to the ligand-centered transitions in the excitation spectra indicates that BDC^{2-} can transfer energy to the Ln^{3+} ions as the indirect excitation of the Ln^{3+} ions through ligand is more effective than the direct excitation of Ln^{3+} ions, hence, BDC^{2-} appears to be suitable as a sensitizer (antenna) for Ln^{3+}. A schematic

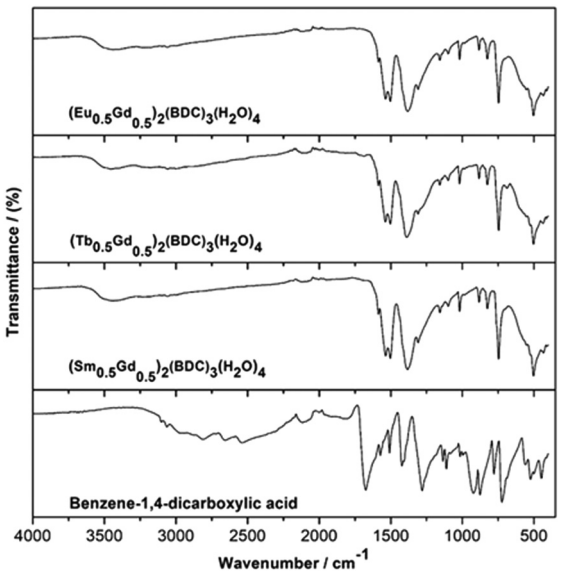

Fig. 5 IR spectra of as-prepared $(Ln_{0.5}Gd_{0.5})_2(BDC)_3(H_2O)_4$ Ln = Sm, Eu and Tb and benzene-1,4-dicarboxylic acid, for comparison.

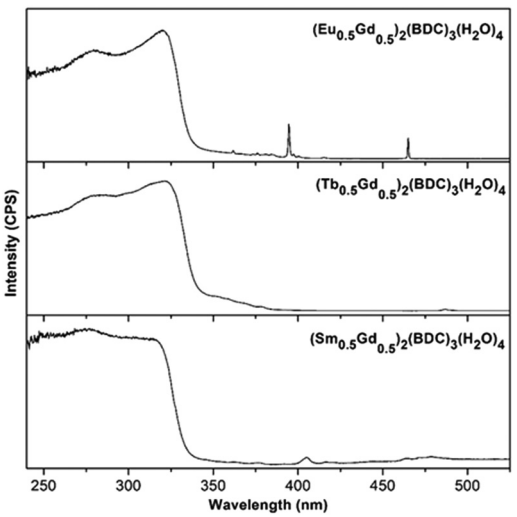

Fig. 6 Excitation spectra of $(Ln_{0.5}Gd_{0.5})_2(BDC)_3(H_2O)_4$ Ln = Eu, Tb, Sm in the solid state at room temperature monitored at 616, 545, and 645 nm, respectively.

energy level diagram showing intramolecular energy transfer processes is presented in Fig. S3 (ESI†).

The emission spectrum of $(Sm_{0.5}Gd_{0.5})_2(BDC)_3(H_2O)_4$ reveals the characteristic bands for the Sm^{3+} ion at 562, 598, 645 and 709 nm corresponding to the $^4G_{5/2}$–^6H_J transitions (J = 5/2, 7/2, 9/2, 11/2) when excited at 315 nm (Fig. 7). The $^4G_{5/2}$–$^6H_{7/2}$ and $^4G_{5/2}$–$^6H_{9/2}$ transitions are most prominent bands and they are responsible for the orange-red colour of emission. The hypersensitive electric dipole $^4G_{5/2}$–$^6H_{9/2}$ transition is sensitive to the symmetry of coordination environment, while the magnetic dipole $^4G_{5/2}$–$^6H_{5/2}$ transition is insensitive to the coordination environment of the Sm^{3+} ion. It is clearly seen from Fig. 7 that the $^4G_{5/2}$–$^6H_{9/2}$ transition is more intense than the $^4G_{5/2}$–$^6H_{5/2}$ transition. This is in agreement with the fact that the Sm^{3+} ions are located at a non-centrosymmetric site.[34]

Upon excitation at 320 nm, the $(Eu_{0.5}Gd_{0.5})_2(BDC)_3(H_2O)_4$ emission spectrum reveals the characteristic Eu^{3+} luminescence originating from the $^5D_0$–^7F_J (J = 0, 1, 2, 3, 4) transitions (Fig. 8). Based on the selection rules of the electric dipole transition, the existence of a single $^5D_0$–$^7F_0$ transition at 580 nm informs that the Eu^{3+} ions occupy a site without inversion symmetry, in agreement with the crystal structure. The weak band at 590 nm ($^5D_0$–$^7F_1$) belongs to a magnetic dipole transition, which is independent of the coordination and local environment of the Eu^{3+} ion. The relative emission intensity of $^5D_0$–$^7F_2$ transition is much higher than the $^5D_0$–$^7F_1$ transition confirming the presence of low symmetry without centre of inversion around the Eu^{3+} ions. Furthermore, the hypersensitive electric dipole $^5D_0$–$^7F_2$ transition centered on 616 nm is the strongest band. This band is dependent on the local environment around Eu^{3+} ions and is responsible for the red emission. The asymmetry ratio (I) of ($^5D_0$–$^7F_2$) to ($^5D_0$–$^7F_1$) was estimated to be 5.08 for $(Eu_{0.5}Gd_{0.5})_2(BDC)_3(H_2O)_4$. No emission band from ligand centered transition could be observed in the emission spectra of either of the Eu^{3+} based complex indicating an efficient operative intramolecular energy transfer from the BDC^{2-} ligand to Eu^{3+} ions.

For $(Tb_{0.5}Gd_{0.5})_2(BDC)_3(H_2O)_4$, under excitation at 323 nm, the typical narrow emission bands of Tb^{3+} ions arising from $^5D_4$–^7F_J (J = 0–6) transitions at 488 ($^5D_4$–$^7F_6$), 545 ($^5D_4$–$^7F_5$), 587 ($^5D_4$–$^7F_4$), 623 ($^5D_4$–$^7F_3$), 651 ($^5D_4$–$^7F_2$), 669 ($^5D_4$–$^7F_1$), and 681 nm ($^5D_4$–$^7F_0$) can be seen (Fig. 9).[33] The hypersensitive $^5D_4$–$^7F_5$ transition is the most intense band and gives a rise to the green emission for both Tb-based MOFs. The splitting observed in this band confirms the low site symmetry around Tb^{3+} ions.

The CIE chromaticity coordinates (x, y) of the mechanochemically synthesized $(Ln_{0.5}Gd_{0.5})_2(BDC)_3(H_2O)_4$ samples calculated from corresponding emission spectra are listed in Table 3. As shown in Fig. 10, the colour coordinates of compounds are located in the orange-red for $(Sm_{0.5}Gd_{0.5})_2(BDC)_3(H_2O)_4$, the red region for $(Eu_{0.5}Gd_{0.5})_2(BDC)_3(H_2O)_4$ and in the green for $(Tb_{0.5}Gd_{0.5})_2(BDC)_3(H_2O)_4$. These values are very close to the reported data by the National Television System committee (NTSC) for primary red (0.630, 0.340) and primary green (0.310, 0.595)

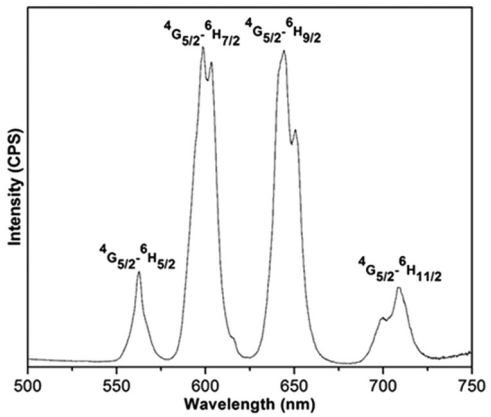

Fig. 7 The emission spectrum of $(Sm_{0.5}Gd_{0.5})_2(BDC)_3(H_2O)_4$ in the solid state at room temperature.

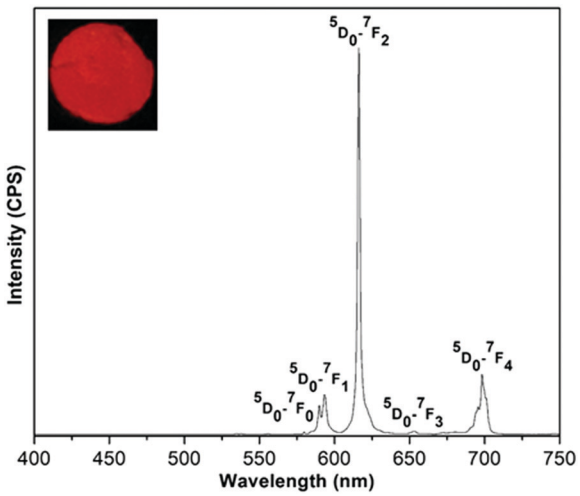

Fig. 8 The emission spectrum of $(Eu_{0.5}Gd_{0.5})_2(BDC)_3(H_2O)_4$ in the solid state at room temperature under excitation with 320 nm. The inset shows luminescence of the sample under UV light (255 nm).

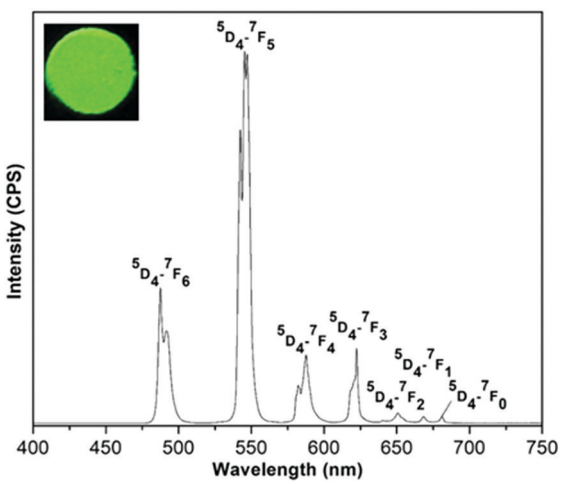

Fig. 9 The emission spectra of $(Tb_{0.5}Gd_{0.5})_2(BDC)_3(H_2O)_4$ in the solid state at room temperature under excitation at 323 nm. The inset shows luminescence of the sample under UV light (255 nm).

Table 3 The CIE chromaticity coordinates (x, y), lifetimes, and quantum yields for $(Ln_{0.5}Gd_{0.5})_2(BDC)_3(H_2O)_4$ Ln = Eu, Tb, Sm complexes

Sample	CIE coordinates (x, y)	Lifetime τ (ms)	Quantum yield (%)
$(Sm_{0.5}Gd_{0.5})_2(BDC)_3(H_2O)_4$	0.539, 0.341	0.062, 0.006	0.1
$(Eu_{0.5}Gd_{0.5})_2(BDC)_3(H_2O)_4$	0.659, 0.336	0.287	2.4
$(Tb_{0.5}Gd_{0.5})_2(BDC)_3(H_2O)_4$	0.322, 0.596	0.811	22

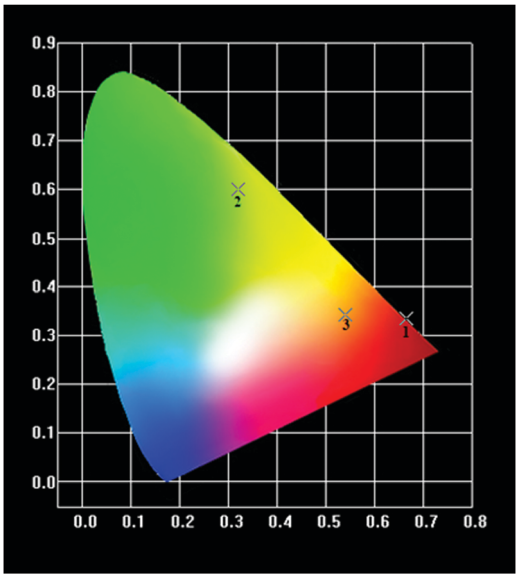

Fig. 10 1931 CIE chromaticity diagram of $(Sm_{0.5}Gd_{0.5})_2(BDC)_3(H_2O)_4$ (3), $(Eu_{0.5}Gd_{0.5})_2(BDC)_3(H_2O)_4$ (1) and $(Tb_{0.5}Gd_{0.5})_2(BDC)_3(H_2O)_4$ (2).

indicating that these materials would be of interest in commercial applications.[35]

The room temperature luminescence lifetimes of $(Ln_{0.5}Gd_{0.5})_2(BDC)_3(H_2O)_4$ Ln = Sm, Eu, Tb, are measured by monitoring the $^4G_{5/2}$–$^6H_{7/2}$ transition for Sm^{3+}, $^5D_0$–$^7F_2$ for Eu^{3+} and $^5D_4$–$^7F_5$ for Tb^{3+}. The decay curves and fit curves are depicted in Fig. 11 and the data are listed in Table 3. The decay curve for $(Sm_{0.5}Gd_{0.5})_2(BDC)_3(H_2O)_4$ had to be fitted by a double-exponential function:

$$I = I_0 + A_1 \exp(-t/\tau_1) + A_2 \exp(-t/\tau_2), \quad (1)$$

whilst the curves for $(Ln_{0.5}Gd_{0.5})_2(BDC)_3(H_2O)_4$ Ln = Eu, Tb could be fitted to a single exponential function as:

$$I = I_0 + A_1 \exp(-t/\tau). \quad (2)$$

On the basis of eqn (1) and (2), and the decay curves presented in Fig. 11, the lifetime values are calculated as τ_1 = 0.062 ms and τ_2 = 0.006 ms for $(Sm_{0.5}Gd_{0.5})_2(BDC)_3(H_2O)_4$, τ = 0.28 ms for $(Eu_{0.5}Gd_{0.5})_2(BDC)_3(H_2O)_4$ and τ = 0.81 ms for $(Tb_{0.5}Gd_{0.5})_2(BDC)_3(H_2O)_4$ and $Tb_2(BDC)_3(H_2O)_4$ (Table 3). It is noteworthy to mention that the single exponential behaviour of decay curve of $(Ln_{0.5}Gd_{0.5})_2(BDC)_3(H_2O)_4$, Ln = Eu, Tb reveals the existence of homogenous chemical environment around the Eu^{3+} and Tb^{3+} ions. In contrast, the decay pattern of $(Sm_{0.5}Gd_{0.5})_2(BDC)_3(H_2O)_4$ shows aside from the expected decay

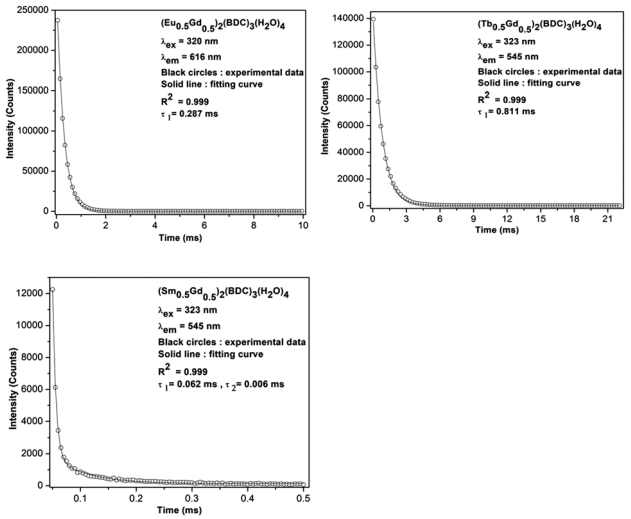

Fig. 11 Room-temperature luminescence decay curves of $(Ln_{0.5}Gd_{0.5})_2(BDC)_3(H_2O)_4$ Ln = Sm, Eu, Tb.

of ions in bulk Sm^{3+} $(Sm_{0.5}Gd_{0.5})_2(BDC)_3(H_2O)_4$ a small contribution of a second, fast decaying species.

The emission quantum yields of the mechanochemically prepared $(Ln_{0.5}Gd_{0.5})_2(BDC)_3(H_2O)_4$ samples were measured in the solid-state by using integrating sphere at room temperature under the excitation wavelength of 323 nm. The recorded values of quantum yields are around 2.4% for $(Eu_{0.5}Gd_{0.5})_2(BDC)_3(H_2O)_4$, 22% for $(Tb_{0.5}Gd_{0.5})_2(BDC)_3(H_2O)_4$, and 0.1% for $(Sm_{0.5}Gd_{0.5})_2(BDC)_3(H_2O)_4$ (Table 3).

The energy transfer mechanism comprises harvesting the light by the ligand then transfer the energy to the excited state of Ln^{3+}. Latva *et al.* reported that the energy difference between the triplet state of ligand and emissive level of Ln^{3+} ions ΔE (T_1–^5D_J) for optimal energy transfer must be around 2500–4000 cm^{-1} for Eu^{3+} and 2500–4500 cm^{-1} for Tb^{3+}.[36] The triplet state energy value for the BDC^{2-} ligand was determined by Zhang *et al.* to be 23 641 cm^{-1}.[37] This value is located above the emitted levels of $^5D_0$ of Eu^{3+} (17 300 cm^{-1}), $^5D_4$ of Tb^{3+} (20 400 cm^{-1}) and $^4G_{5/2}$ of Sm^{3+} (18 021 cm^{-1}) with energy differences of ΔE being 6341 cm^{-1} for $(Eu_{0.5}Gd_{0.5})_2(BDC)_3(H_2O)_4$, 3241 cm^{-1} for $(Tb_{0.5}Gd_{0.5})_2(BDC)_3(H_2O)_4$ and 5620 cm^{-1} for $(Sm_{0.5}Gd_{0.5})_2(BDC)_3(H_2O)_4$. Therefore, the longer lifetime and higher quantum yield of $(Tb_{0.5}Gd_{0.5})_2(BDC)_3(H_2O)_4$ compared to $(Eu_{0.5}Gd_{0.5})_2(BDC)_3(H_2O)_4$, and $(Sm_{0.5}Gd_{0.5})_2(BDC)_3(H_2O)_4$ can be explained on the basis of the respective ΔE, which is in the ideal energy difference range for an effective energy transfer only for the Tb-containing compound. In the case of the Sm^{3+} based compound, the short lifetime and the nearly complete quenching of emission can be attributed to the large ΔE (T_1–$^5G_{5/2}$) value as well as the small gaps between the emitting $^5G_{5/2}$ level and final the ^6H_J levels (about 7500 cm^{-1}), where nonradiative deactivation is favoured.

Fig. 12 shows the temperature dependent dc-magnetic susceptibility for all the three samples measured in two different fields: 100 Oe and 1 kOe using two protocols namely ZFC, in which samples were cooled down to 5 K in zero magnetic field

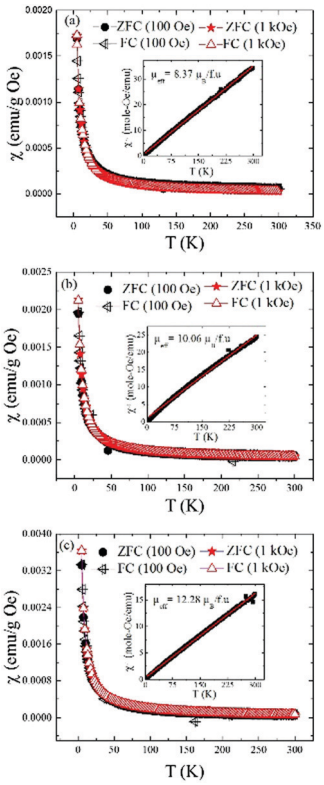

Fig. 12 Temperature dependent dc magnetic susceptibility plots for as-synthesized $(Ln_{0.5}Gd_{0.5})$-BDC MOFs. The data shown were collected in the zero-field cooled (ZFC) and field cooled (FC) condition on heating under the applied magnetic field of 100 Oe and 1 kOe for Ln = (a) Sm, (b) Eu and (c) Tb respectively. The insets show the inverse susceptibility plots (black symbols) and the Curie–Weiss fits (red).

and FC in which samples were cooled down to 5 K in the presence of magnetic field. Magnetic data were recorded during heating cycles for each protocol. The dc-susceptibility was calculated as $\chi = M/H$. For all the samples, $\chi(T)$ increases continuously with decreasing temperature and shows the same trend irrespective of measurement protocols and magnetic field which indicate absence of any thermomagnetic irreversibility typically seen in materials with long-range magnetic ordering.[38] Similar *M vs. T* behavior was also seen previously in the mechanochemically synthesized lanthanide MOFs with MIL-78 structure.[17] The paramagnetic behavior of the samples were further verified by linear χ^{-1} *vs. T* curves passing through $T = 0$ K in accordance with Curie–Weiss law (see insets in Fig. 12a–c). The effective magnetic moments, μ_{eff} for the samples as mentioned in insets were calculated from the slope of χ^{-1} *vs. T* plots. For $(Ln_{0.5}Gd_{0.5})$-BDC MOF with Ln = Sm and Tb, the experimental μ_{eff} (8.37 and 12.28 μ_B per f.u. respectively) are very close to the theoretical values (7.99 and 12.56 μ_B per f.u.), considering 3+ oxidation states for Ln atoms. However, for Ln = Eu, the value is slightly higher than the theoretical (10.06 *vs.* 7.94 μ_B per f.u.). This is not surprising because even for Eu^{3+} the experimentally obtained μ_{eff} is often reported to be much higher compared to its theoretical value of 0 μ_B.[39] A comparison of experimental and theoretical values of μ_{eff} for four relevant lanthanide atoms are shown in Fig. S4 in ESI.†

Conclusions

In summary, three new coordination polymers have been successfully synthesized from lanthanide carbonates and benzene-1,4-dicarboxylate by solvent-free mechanochemistry. Powder X-ray diffraction measurements confirmed that the compounds are isostructural with $Tb_2(1,4\text{-BDC})_3(H_2O)_4$. The luminescent properties of $(Ln_{0.5}Gd_{0.5})_2(BDC)_3(H_2O)_4$ Ln = Eu, Sm, Tb were investigated in the solid-state at room temperature. The absence of any emission from ligand in the emission spectra demonstrates the utility of BDC^{2-} ligand as a good sensitizer. This can be explained from the position of the ligand T-level with respect to the emitting Ln^{3+} ions levels. The observed lifetimes range from 0.811 ms for $(Tb_{0.5}Gd_{0.5})_2(BDC)_3(H_2O)_4$ and 0.287 ms for $(Eu_{0.5}Gd_{0.5})_2(BDC)_3(H_2O)_4$ to 0.006 ms for $(Sm_{0.5}Gd_{0.5})_2(BDC)_3(H_2O)_4$ and the quantum yields vary from 22% for $(Tb_{0.5}Gd_{0.5})_2(BDC)_3(H_2O)_4$ to 0.1% for $(Sm_{0.5}Gd_{0.5})_2(BDC)_3(H_2O)_4$ to. The superior luminescent properties of $(Tb_{0.5}Gd_{0.5})_2(BDC)_3(H_2O)_4$ complex can be ascribed to the suitable energy gap between the lowest triplet energy level of BDC^{2-} ligand with the emissive level of Tb^{3+} which allows for the most efficient ligand-to-metal energy transfer. No long-range magnetic ordering is observed in any of the as-synthesized $(Ln_{0.5}Gd_{0.5})_2(BDC)_3(H_2O)_4$ MOFs. The results presented here demonstrate that solvent-free mechanochemical synthesis is well suited for synthesis of not only single metal MOFs but also for the synthesis of solid-solutions of two or perhaps more than two lanthanide elements. This opens up an opportunity to tailor the composition and precisely control the dopant concentrations in the luminescent materials that is highly critical for their optimal performance.

Experimental

Materials

Precursors $Eu_2(CO_3)_3{\cdot}4H_2O$, $Gd_2(CO_3)_3{\cdot}4H_2O$, $Sm_2(CO_3)_3{\cdot}4H_2O$, $Tb_2(CO_3)_3{\cdot}6H_2O$, and benzene-1,4-dicarboxylic acid (terephthalic acid, $C_6H_4(COOH)_2$) were purchased from Alfa Aesar and were used without further purification.

Synthesis of $(Ln_{0.5}Gd_{0.5})_2(1,4\text{-BDC})_3(H_2O)_4$

$(Ln_{0.5}Gd_{0.5})$-BDC MOFs were prepared by mechanochemical reaction of mixtures of benzene-1,4-dicarboxylic acid with the respective rare-earth carbonate hydrates $Ln_2(CO_3)_3{\cdot}xH_2O$ (Ln = Sm, Eu, Tb) and $Gd_2(CO_3)_3{\cdot}4H_2O$ taken in 3 : 1 : 0 molar ratio for $Ln_2(BDC)_3(H_2O)_4$ and 3 : 0.5 : 0.5 molar ratio for $(Ln_{0.5}Gd_{0.5})_2(BDC)_3(H_2O)_4$. In a typical synthesis, a total of 1 g of the stoichiometric mixture was placed into a ~65 ml hardened steel container together with two 12.7 mm and four 6.35 mm grinding stainless steel balls (ball-to-sample ratio close to 18 : 1) and ball-milled in a SPEX 8000M shaker mill for up to 2 h. All milling experiments were performed under argon atmosphere.

Characterization

Powder X-ray diffraction (XRD). The XRD measurements were carried out on a PANalytical X'PERT powder diffractometer with an Xcelerator detector employing Cu-Kα1 radiation

(λ = 0.15406 nm) in the 2θ range from 5° to 80° with a step size of 0.02°.

Thermogravimetric analysis (TGA) and differential scanning calorimetry (DSC). The TGA and DSC data were collected at a heating rate of 10 °C min^{-1} in alumina crucibles from room temperature to 1000 °C using a Netzsch STA449 F1 Jupiter.

X-ray photoemission spectroscopy (XPS). The XPS measurements were performed in a stainless-steel ultrahigh vacuum chamber (PerkinElmer, model 5500, base pressure <10–10 mbar). XPS data were acquired on a physical electronic 5500 multi-technique system with standard aluminium source. The analysis spot size was 1 × 1 mm^2. Samples were mounted on a double sided Scotch© tape. The binding energies in the XPS spectra are calibrated against the C-1s signal (284.8 eV) corresponding to adventitious physisorbed carbon dioxide.

IR spectroscopy. Attenuated total reflection (ATR) spectroscopy was carried out on an Alpha ATR spectrometer equipped with a diamond crystal (Bruker, Karlsruhe, D). Solid samples were pressed on the crystal with diamond surface to ensure contact.

UV-Vis spectroscopy. UV-Vis spectra were measured at room temperature on a Cary 5000 spectrometer (Varian, Palo Alto, US) in reflection mode.

Fluorescence spectroscopy. Excitation and emission spectra were measured at room temperature on a HORIBA Jobin Yvon Fluorolog 3-222 spectrofluorometer, using a 450 W xenon arc lamp and a R928P PMT detector. The decay curve measurements were obtained by using the same instrument using a xenon flash lamp for excitation.

Transmission electron microscopy (TEM). TEM imaging was performed on a FEI Titan Themis 300 probe-corrected scanning transmission electron microscope (STEM), under an accelerating voltage of 200 kV. Samples were ground to fine powders, dispersed in ethanol, and drop-casted on a Cu TEM grid. High-angle-annular-dark-field (HAADF) scanning transmission electron microscopy (HAADF) images were recorded with a collection angle of 99–200 mrad. Energy dispersive X-ray spectroscopy (EDS) was collected using a Super-X EDX detector.

Magnetic measurements. The magnetic properties were measured using the superconducting quantum interference device (SQUID, MPMS XL, Quantum Design, USA). The temperature (T) dependence of magnetization (M) data were collected under zero field cooled (ZFC) and field cooled cooling (FCC) conditions for all three $(Ln_{0.5}Gd_{0.5})_2(BDC)_3(H_2O)_4$ MOFs.

Conflicts of interest

There are no conflicts to declare.

Acknowledgements

Ames Laboratory is operated for the U.S. Department of Energy (DOE) by Iowa State University of Science and Technology under contract No. DE-AC02-07CH11358. Research on mechanochemical synthesis, structural and magnetic characterization was supported by the Division of Materials Sciences and Engineering of Basic Energy Sciences Program of the Office of Science of the U.S. Department of Energy. Research on optical properties was supported by the National Science Foundation, NSF, grant CHE-1465071. AVM acknowledges support from the Swedish Royal Academy of Science through the Göran Gustafsson prize in Chemistry and support through Vetenskapsrådet (research grant 2016-05405).

Notes and references

1 J. C. G. Bünzli, *Coord. Chem. Rev.*, 2015, **293**, 19–47.
2 M. A. Katkova and M. N. Bochkarev, *Dalton Trans.*, 2010, **39**, 6599–6612.
3 L. D. Carlos, R. A. Ferreira, V. de Zea Bermudez, B. Julian-Lopez and P. Escribano, *Chem. Soc. Rev.*, 2011, **40**, 536–549.
4 Ó. Guzmán-Méndez, F. González, S. Bernès, M. Flores-Álamo, J. Ordóñez-Hernández, H. García-Ortega, J. Guerrero, W. Qian, N. Aliaga-Alcalde and L. Gasque, *Inorg. Chem.*, 2018, **57**, 908–911.
5 S. Faulkner, S. J. Pope and B. P. Burton-Pye, *Appl. Spectrosc. Rev.*, 2005, **40**, 1–31.
6 Z. Wang, D. Ananias, A. Carné-Sánchez, C. D. Brites, I. Imaz, D. Maspoch, J. Rocha and L. D. Carlos, *Adv. Funct. Mater.*, 2015, **25**, 2824–2830.
7 Z. Hu, B. J. Deibert and J. Li, *Chem. Soc. Rev.*, 2014, **43**, 5815–5840.
8 (*a*) S.-J. Liu, S.-D. Han, J.-P. Zhao, J. Xu and X.-H. Bu, *Coord. Chem. Rev.*, 2019, **394**, 39–52; (*b*) S.-J. Liu, C. Cao, C.-C. Xie, T.-F. Zheng, X.-L. Tong, J.-S. Liao, J.-L. Chen, H.-R. Wen, Z. Chang and X.-H. Bu, *Dalton Trans.*, 2016, **45**, 9209–9215.
9 Y. Cui, Y. Yue, G. Qian and B. Chen, *Chem. Rev.*, 2011, **112**, 1126–1162.
10 S. I. Weissman, *J. Chem. Phys.*, 1942, **10**, 214–217.
11 E. G. Moore, A. P. Samuel and K. N. Raymond, *Acc. Chem. Res.*, 2009, **42**, 542–552.
12 N. Stock and S. Biswas, *Chem. Rev.*, 2011, **112**, 933–969.
13 K. D. Harris, *Nat. Chem.*, 2013, **5**, 12–14.
14 W. Liu, K. Zhu, S. J. Teat, B. J. Deibert, W. Yuan and J. Li, *J. Mater. Chem. C*, 2017, **5**, 5962–5969.
15 D. Yuan, G. S. Yi and G. M. Chow, *J. Mater. Res.*, 2009, **24**, 2042–2050.
16 N. K. Singh, M. Hardi and V. P. Balema, *Chem. Commun.*, 2013, **49**, 972–974.
17 N. K. Singh, S. Gupta, V. K. Pecharsky and V. P. Balema, *J. Alloys Compd.*, 2017, **696**, 118–122.
18 M. Klimakow, P. Klobes, A. F. Thünemann, K. Rademann and F. Emmerling, *Chem. Mater.*, 2008, **47**, 5216–5221.
19 J.-L. Do and T. Friščić, *ACS Cent. Sci.*, 2017, **3**, 13–19.
20 P. Zhang and S. Dai, *J. Mater. Chem. A*, 2017, **5**, 16118–16127.
21 T. M. Reineke, M. Eddaoudi, M. Fehr, D. Kelley and O. M. Yaghi, *J. Am. Chem. Soc.*, 1999, **121**, 1651–1657.
22 R. D. Shannon, *Acta Crystallogr., Sect. A: Cryst. Phys., Diffr., Theor. Gen. Crystallogr.*, 1976, **32**, 751–767.
23 L.-N. Jin, Q. Liu, Y. Lu and W.-Y. Sun, *CrystEngComm*, 2012, **14**, 3515–3520.

24 L. Pan, N. Zheng, Y. Wu, S. Han, R. Yang, X. Huang and J. Li, *Inorg. Chem.*, 2001, **40**, 828–830.
25 R. Vercaemst, D. Poelman, L. Fiermans, R. L. Van Meishaeghe, W. H. Laflere and F. Cardon, *J. Electron Spectrosc. Relat. Phenom.*, 1995, **74**, 45–56.
26 S. Kumar, R. Prakash, R. J. Choudhary and D. M. Phase, *Mater. Res. Bull.*, 2015, **70**, 392–396.
27 W. Cartas, R. Rai, A. Sathe, A. Schaefer and J. F. Weaver, *J. Phys. Chem. C*, 2014, **118**, 20916–20926.
28 L. Song and M. Rongjun, *J. Cryst. Growth*, 1996, **169**, 190–192.
29 B. Vallina, J. D. Rodriguez-Blanco, A. P. Brown, J. A. Blanco and L. G. Benning, *J. Nanopart. Res.*, 2013, **15**, 1438.
30 A. Sungur and M. Kizilyalli, *J. Less-Common Met.*, 1983, **93**, 419–423.
31 R. J. Batrice, A. K. Adcock, P. M. Cantos, J. A. Bertke and K. E. Knope, *Cryst. Growth Des.*, 2017, **17**, 4603–4612.
32 A. Gilbert and J. Baggott, *Essentials of Molecular Photochemistry*, CRC Press, Boca Raton, FL, 1991, pp. 87–89.
33 G. H. Dieke and H. M. Crosswhite, *Appl. Opt.*, 1963, **2**, 675–686.
34 V. Haquin, M. Etienne, C. Daiguebonne, S. Freslon, G. Calvez, K. Bernot, L. Le Pollès, S. E. Ashbrook, M. R. Mitchell, J.-C. Bünzli, S. V. Eliseeva and O. Guillou, *Eur. J. Inorg. Chem.*, 2013, 3464–3476.
35 L. De Marsh, TV Display Phosphors/Primaries – Some History, *SMPTE J.*, 1993, 1095–1098.
36 M. Latva, H. Takalo, V. Mukkala, C. Matachescu, J. Rodriguez-Ubis and J. Kankare, *J. Lumin.*, 1997, **75**, 149–169.
37 H.-J. Zhang, R.-Q. Fan, P. Wang, X.-M. Wang, W. Chen, X.-B. Zheng, K. Li and Y.-L. Yang, *J. Inorg. Organomet. Polym. Mater.*, 2014, **24**, 624–632.
38 F.-S. Guo, Y.-C. Chen, J.-L. Liu, J.-D. Leng, Z.-S. Meng, P. Vrabel, M. Orendac and M.-L. Tong, *Chem. Commun.*, 2012, **48**, 12219–12221.
39 R. L. Carlin, *Magnetochemistry*, Springer, NY, 1986, ch. 9.

